Energy and centrality dependence of $\bar{p}$ and p production and the $\bar{\Lambda}/\bar{p}$ ratio in Pb+Pb collisions between 20*A* GeV and 158*A* GeV

C. Alt,[9] T. Anticic,[21] B. Baatar,[8] D. Barna,[4] J. Bartke,[6] L. Betev,[10] H. Białkowska,[19] C. Blume,[9] B. Boimska,[19] M. Botje,[1] J. Bracinik,[3] R. Bramm,[9] P. Buncić,[10] V. Cerny,[3] P. Christakoglou,[2] O. Chvala,[14] J. G. Cramer,[16] P. Csató,[4] P. Dinkelaker,[9] V. Eckardt,[13] D. Flierl,[9] Z. Fodor,[4] P. Foka,[7] V. Friese,[7] J. Gál,[4] M. Gaździcki,[9,11] V. Genchev,[18] G. Georgopoulos,[2] E. Gładysz,[6] K. Grebieszkow,[20] S. Hegyi,[4] C. Höhne,[7] K. Kadija,[21] A. Karev,[13] M. Kliemant,[9] S. Kniege,[9] V. I. Kolesnikov,[8] E. Kornas,[6] R. Korus,[11] M. Kowalski,[6] I. Kraus,[7] M. Kreps,[3] A. Laslo,[4] M. van Leeuwen,[1] P. Lévai,[4] L. Litov,[17] B. Lungwitz,[9] M. Makariev,[17] A. I. Malakhov,[8] M. Mateev,[17] G. L. Melkumov,[8] A. Mischke,[1] M. Mitrovski,[9] J. Molnár,[4] St. Mrówczyński,[11] V. Nicolic,[21] G. Pálla,[4] A. D. Panagiotou,[2] D. Panayotov,[17] A. Petridis,[2] M. Pikna,[3] D. Prindle,[16] F. Pühlhofer,[12] R. Renfordt,[9] C. Roland,[5] G. Roland,[5] M. Rybczyński,[11] A. Rybicki,[6,10] A. Sandoval,[7] N. Schmitz,[13] T. Schuster,[9] P. Seyboth,[13] F. Siklér,[4] B. Sitar,[3] E. Skrzypczak,[20] G. Stefanek,[11] R. Stock,[9] C. Strabel,[9] H. Ströbele,[9] T. Susa,[21] I. Szentpétery,[4] J. Sziklai,[4] P. Szymanski,[10,19] V. Trubnikov,[19] D. Varga,[4,10] M. Vassiliou,[2] G. I. Veres,[4,5] G. Vesztergombi,[4] D. Vranić,[7] A. Wetzler,[9] Z. Włodarczyk,[11] I. K. Yoo,[15] and J. Zimányi[4]

(NA49 Collaboration)

[1]*NIKHEF, Amsterdam, Netherlands*
[2]*Department of Physics, University of Athens, Athens, Greece*
[3]*Comenius University, Bratislava, Slovakia*
[4]*KFKI Research Institute for Particle and Nuclear Physics, Budapest, Hungary*
[5]*MIT, Cambridge, Massachusetts, USA*
[6]*Institute of Nuclear Physics, Cracow, Poland*
[7]*Gesellschaft für Schwerionenforschung (GSI), Darmstadt, Germany*
[8]*Joint Institute for Nuclear Research, Dubna, Russia*
[9]*Fachbereich Physik der Universität, Frankfurt, Germany*
[10]*CERN, Geneva, Switzerland*
[11]*Institute of Physics Świetokrzyska Academy, Kielce, Poland*
[12]*Fachbereich Physik der Universität, Marburg, Germany*
[13]*Max-Planck-Institut für Physik, Munich, Germany*
[14]*Institute of Particle and Nuclear Physics, Charles University, Prague, Czech Republic*
[15]*Department of Physics, Pusan National University, Pusan, Republic of Korea*
[16]*Nuclear Physics Laboratory, University of Washington, Seattle, WA, USA*
[17]*Atomic Physics Department, Sofia University, St. Kliment Ohridski, Sofia, Bulgaria*
[18]*Institute for Nuclear Research and Nuclear Energy, Sofia, Bulgaria*
[19]*Institute for Nuclear Studies, Warsaw, Poland*
[20]*Institute for Experimental Physics, University of Warsaw, Warsaw, Poland*
[21]*Rudjer Boskovic Institute, Zagreb, Croatia*

(Received 20 December 2005; published 24 April 2006)

The transverse mass m_t distributions for antiprotons are measured at midrapidity for minimum bias Pb+Pb collisions at 158*A* GeV and for central Pb+Pb collisions at 20*A*, 30*A*, 40*A*, and 80*A* GeV beam energies in the fixed target experiment NA49 at the CERN SPS. The rapidity density dn/dy, inverse slope parameter T, and mean transverse mass $\langle m_t \rangle$ derived from the m_t distributions are studied as a function of the incident energy and the collision centrality and compared to the relevant data on proton production. The shapes of the m_t distributions of $\bar{p}$ and p are very similar. The ratios of the particle yields, $\bar{p}/p$ and $\bar{\Lambda}/\bar{p}$, are also analyzed. The $\bar{p}/p$ ratio exhibits an increase with decreasing centrality and a steep rise with increasing beam energy. The $\bar{\Lambda}/\bar{p}$ ratio increases beyond unity with decreasing beam energy.

DOI: 10.1103/PhysRevC.73.044910 PACS number(s): 25.75.Dw

I. INTRODUCTION

Copious antibaryon as well as strangeness production in relativistic heavy ion collisions relative to the corresponding yields observed in elementary hadronic interactions have been suggested as signatures of the QCD phase transition to a deconfined partonic state, the quark-gluon plasma [1,2]. The enhancement was expected to arise from gluon fragmentation into quark-antiquark pairs which is believed to have a significantly lower threshold than baryon-antibaryon and strange-antistrange hadron pair production channels. More generally, such enhancements should be a consequence of the creation of a large volume of high energy density matter, uniquely characteristic of central relativistic nuclear collisions [2].

Meanwhile, in the net baryon-rich systems, significant annihilation losses could occur before antibaryons escape the collision volume. Thus, a systematic study of antiproton

production has been proposed as an indirect way of measuring the baryon density created at the instant of hadron formation [3]. The latter is related to the degree of baryon stopping achieved during the early interpenetration phase of the collision. It has also been pointed out that antiprotons can be regenerated in multimeson reactions during the final hadron gas stage [4,5]. Experimentally, the interplay between baryon stopping, baryon pair production, and antibaryon annihilation can be assessed through the measurement of antiproton and proton yields, and the yield ratios. This is the subject of the study presented in this paper for the CERN super proton synchroton (SPS) energy range.

As no antibaryons are contained in the initial nuclear projectiles, their yields and spectra are determined predominantly by processes occurring subsequent to the primordial baryon stopping mechanisms. Of particular interest is the ratio of antilambda $\bar{\Lambda}$ to antiproton $\bar{p}$ which, intuitively, reflects the relative abundances of antistrange to antilight quarks at the stage of formation of the finally observed antibaryons. The $\bar{\Lambda}/\bar{p}$ production ratio amounts to about 0.25 in elementary hadron collisions at SPS energy [6], but it has been found to significantly exceed unity in previous studies of central nucleus-nucleus collisions at alternating-gradient synchroton (AGS) energies [7–9]. From the top SPS energy ($\sqrt{s_{NN}} =$ 17.3 GeV) to the energy ($\sqrt{s_{NN}} = 130$ GeV) available at the BNL Relativistic Heavy Ion Collider (RHIC), this ratio is known to stay at about unity [10,11], a value also obtained as an upper limit (reflecting the general observation on strangeness enhancement in central A+A collisions) in recent theoretical studies employing statistical and microscopic transport models [12–16]. As, in particular, the latter dynamical models attempt to incorporate both the effects of primordial net baryon stopping and of antibaryon annihilation (subsequent to the initial antibaryon formation phase) [15–18] the observation at top AGS energies, of $\bar{\Lambda}/\bar{p}$ significantly exceeding unity, remains a puzzle. This effect might be related to the recent observation of a steep maximum of the K^+/π^+ ratio, occurring in the vicinity of top AGS to lowest SPS energy [19,20]. Similar to the $\bar{\Lambda}/\bar{p}$ ratio, the K^+/π^+ ratio also refers to the antistrange to antilight quark abundance ratio, prevailing at hadron formation.

The paper presents an extension of the previously known $\bar{p}/p$ production ratio to the lower CERN SPS energies. New measurements of antiproton yields in centrality selected Pb+Pb collisions at beam energies of 158A GeV ($\sqrt{s_{NN}} =$ 17.3 GeV) and in central Pb+Pb collisions at 20A, 30A, 40A, and 80A GeV ($\sqrt{s_{NN}} = 6.3$, 7.6, 8.7, and 12.3 GeV, respectively) were performed bridging the gap between the data at top AGS and SPS energies. Previously published proton yield measurements of NA49 at 40A, 80A, and 158A GeV [21] are extended to 20A and 30A GeV beam energies. The $\bar{\Lambda}/\bar{p}$ ratios are then obtained using recent $\bar{\Lambda}$ results from NA49 [22] and NA57 [23].

II. EXPERIMENTAL METHOD

NA49 is a fixed target experiment at CERN with a large acceptance detector [24] using external SPS beams of nuclei and hadrons. The produced charged particles were detected in four large-volume time projection chambers (TPCs). Two of them (VTPCs) are located inside the magnetic field; the two others (MTPCs) are downstream of the magnets on either side of the beamline. The TPCs provide precise tracking and particle identification in a wide range of phase space based on the measured momentum and the specific energy loss dE/dx in the TPC gas with about 4% resolution.

Two time-of-flight (TOF) detector walls containing 891 scintillator pixels each are situated symmetrically behind the TPCs on both sides of the beam. The average overall time resolution of these detectors is 60–70 ps. In the present analysis, the identification of antiprotons was primarily accomplished by the TOF measurement, the dE/dx information from the large TPCs being employed to reduce the background of charged pions and kaons in the mass spectrum. To demonstrate the identification capability, a sample of the particle mass spectra obtained from measured momenta and time of flight are shown in Fig. 1.

Online event characterization and triggering is accomplished by beam definition detectors located in the beamline upstream of the target and interaction counters, and a calorimeter downstream of the target. The data samples were recorded with two trigger settings, providing the selection of central and minimum bias events.

Central Pb+Pb collisions were selected by requesting the energy deposited in the projectile fragmentation region to be lower than a given threshold. This was achieved with a zero degree calorimeter (ZDC) located downstream of the detector measuring the energy E_{ZDC} of the remaining projectile fragments and spectator protons and neutrons. The upper limit on the energy in the ZDC was set to accept the 12% most central events at 158A GeV and 7% at 20A, 30A, 40A, and 80A GeV from all inelastic Pb+Pb collisions. For the top SPS energy, the 5% most central interactions were selected offline.

A gas Cherenkov counter provided a minimum bias trigger for Pb+Pb collisions. It was placed in the gas region immediately behind the target to veto noninteracting projectiles. Triggering was accomplished by placing an upper threshold on the signal from this Cherenkov counter in coincidence with a valid signal from the beam detectors. Additionally, offline cuts were made on the position of the fitted primary vertex along the beam direction to minimize the fraction of nontarget background events.

III. DATA ANALYSIS AND RESULTS

For the analysis of 158A GeV Pb+Pb collisions, the data samples of 450 000 central and 400 000 minimum bias events were used. In order to study the centrality dependence, the data were segregated into six centrality classes selected by subdividing the range of the total energy measured in the ZDC. For each centrality bin, the cross section was determined experimentally and corresponded to an interval in the inelastic Pb+Pb collision cross section. The resulting intervals, assuming a total inelastic cross section $\sigma_{\mathrm{inel}} = 7.15$ barns, are listed in Table I. The initial geometry of nucleus-nucleus collisions is usually characterized by the number of wounded nucleons

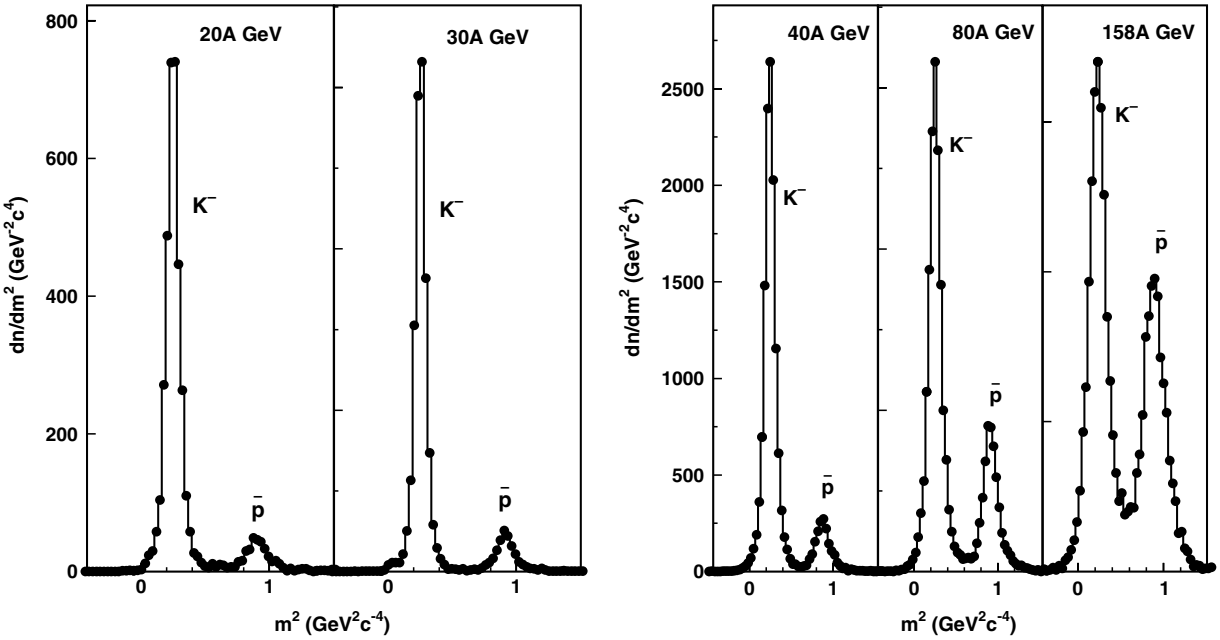

FIG. 1. Mass squared histograms for TOF-identified kaons and antiprotons in Pb+Pb reactions at 20*A*, 30*A*, 40*A*, 80*A*, and 158*A* GeV beam energies. dE/dx cuts have been applied to the data to reject most of the pions. The particle momenta range from 3 to 10 GeV/c.

N_{wound} which essentially represents the number of nucleons in the geometric overlap volume of the colliding nuclei. The values of N_{wound} as a function of impact parameter b and inelastic cross section range are obtained from Glauber model calculations [25]. The resulting averages $\langle N_{\text{wound}}\rangle$ and $\langle b\rangle$ for the six inelastic cross section intervals of this analysis are shown in Table I. The value of σ_{inel} is not known precisely. An estimated uncertainty of 5% leads to a systematic uncertainty in $\langle N_{\text{wound}}\rangle$ of 1% (10%) for central (peripheral) collisions. Note that bin 6 suffers from a trigger bias, i.e., the minimum bias trigger only accepts about 35% of the events in this centrality range. The listed values of $\langle N_{\text{wound}}\rangle$ and $\langle N_{\text{part}}\rangle$ are not averages for the 43–100% cross section interval, but refer to those events accepted by the trigger. Since the quantity N_{wound} is not a direct observable, previous publications of NA49 also employed the number of participants N_{part}, which counts all the nucleons from the incident nuclei involved in any hadronic reaction (including those hit by a scattered or produced particle). N_{part} can be estimated from the baryons and antibaryons measured by the detector or from the spectator energy deposited in the ZDC [26–28]. For comparison, $\langle N_{\text{part}}\rangle$ is also listed in Table I; the values differ significantly from $\langle N_{\text{wound}}\rangle$ for peripheral collisions.

TABLE I. Six centrality classes in 158*A* GeV Pb+Pb collisions, listing the covered range in fraction of total cross section σ_{inel}, mean numbers of participating $\langle N_{\text{part}}\rangle$ and wounded $\langle N_{\text{wound}}\rangle$ nucleons, and impact parameter $\langle b\rangle$ for corresponding cross sections. Standard deviations of distributions of N_{wound} and b for the respective centrality bins are also quoted.

Centrality bin	Fraction of σ_{inel}(%)	$\langle N_{\text{part}}\rangle$	$\langle N_{\text{wound}}\rangle$	$\langle b\rangle$ (fm)
1	0–5	366	357 ± 22	2.3 ± 0.9
2	5–12	309	288 ± 28	4.5 ± 0.8
3	12–23	242	211 ± 30	6.4 ± 0.8
4	23–33	178	146 ± 25	8.1 ± 0.8
5	33–43	132	99 ± 22	9.5 ± 0.8
6	43–100	85	42 ± 16	11.8 ± 1.0

For the reconstruction of charged tracks, a global tracking scheme was used which combined all track segments reconstructed in the TPCs that belong to the same particle. For each event, the primary vertex was determined from the intersection of reconstructed tracks. Events in which no primary vertex was found were rejected. Event vertex as well as track quality cuts were applied in order to select the events for further analysis. The event vertex had to lie within ± 1 cm of the target foil position. The global track was required to comprise track segments in the MTPC and at least one of the VTPCs. The reconstructed tracks having momentum and dE/dx information were extrapolated to the TOF detector wall and assigned a mass squared value m^2 derived from the momentum, flight path, and time-of-flight measurements. Furthermore, cuts were applied to eliminate tracks which impinge close to the edges of the scintillator tiles or which point to tiles hit by more than one track or which show a signal from event-correlated γ-conversion pairs in the scintillator. The corresponding inefficiency was determined experimentally from the TPC tracking data (edge and double hit) and the charge measurements in the TOF scintillators (γ conversion) and amounts to 25% on average, with a maximum of 30% in the region of the TOF wall closest to the beam. The relevant corrections have been applied to the measured particle yields.

Next, antiprotons were selected, and their transverse mass m_t distributions reconstructed. The tracks were subjected to identification cuts applied to the measured dE/dx and m^2

values in order to simultaneously maximize the number of antiprotons and minimize the background stemming mostly from pions and kaons. Correction factors for the $\bar{p}$ yield due to the cuts were estimated from the experimental dE/dx and m^2 distributions using parametrized descriptions obtained from a fit. The mass squared distributions were described by a sum of a Gaussian distribution for the $\bar{p}$ signal and a background with two components: an exponentially falling contribution from the tails of K^- and π^- bands, and a flat random distribution due to misidentified particles. The energy loss dE/dx is well described by a sum of Gaussian distributions. The fits were performed for each (p_t, p) bin of width $\Delta p_t = 0.2$ GeV/c and $\Delta p = 1.0$ GeV/c in the full kinematic range of antiprotons accepted by the TOF detector: $0 < p_t < 1.7$ GeV/c and $3.0 < p < 10.0$ GeV/c. The correction factors for the antiproton loss and background contamination due to the cuts were then determined separately for each (p_t, p) bin. They were negligible in the momentum range up to $p = 6.0$ GeV/c and reached about 15% at large momenta.

Some fraction of the measured antiprotons are the daughters of weak decays of strange antibaryons, mainly $\bar{\Lambda}$, including those from electromagnetic decay of $\bar{\Sigma}^0$ which are experimentally indistinguishable from primary $\bar{\Lambda}$. This so-called feeddown was evaluated from a GEANT-based Monte Carlo simulation of $\bar{\Lambda}$ and $\bar{\Sigma}$ decays in the NA49 detector, including detector response simulation and reconstruction of the charged decay products. This procedure takes into account the probability for a secondary antiproton to be reconstructed as a track from the primary vertex. As input for the simulation, $\bar{\Lambda}$ yields and phase space distributions measured by the SPS experiments were employed. The $\bar{\Lambda}$ yields in each centrality bin were derived using the $\bar{\Lambda}$ centrality dependence obtained in NA57 [23] scaled to the $\bar{\Lambda}$ yield in central Pb+Pb collisions measured by NA49 [22]. The relatively small fraction of antiprotons from $\bar{\Sigma}^-$ decays was calculated using the RQMD model [29] simulation. The calculated m_t spectra of feeddown antiprotons are well described by an exponential function. The inverse slope parameter of these spectra gradually changes from 265 to 215 MeV from the most central to the peripheral bins, respectively. The overall contribution of feeddown antiprotons was found to vary from 25% in peripheral to 35% in central collisions. These values also contain the antiprotons from doubly strange cascades.

The correction factor for geometrical acceptance was calculated using the GEANT package for tracking particles and dedicated NA49 software to simulate the detector response. The track reconstruction efficiency in the TPCs for primary p and $\bar{p}$ was determined by embedding simulated particle tracks into raw data events, which were then passed through the same reconstruction procedure as the real data. It was found to be nearly 100% in the kinematic range covered by the TOF acceptance.

The discussed corrections have been applied to the data in each rapidity-transverse mass (y, m_t) bin. The transverse mass m_t ($m_t = \sqrt{p_t^2 + m^2}$) spectra for antiprotons were then obtained by integrating the data over the measured rapidity region. The resulting $\bar{p}$ spectra as well as previously published proton spectra [21] in centrality selected 158A GeV Pb+Pb collisions at $2.4 < y < 2.8$ ($y_{\text{c.m.}} = 2.9$) are shown in Fig. 2 along with a fit function of the form

$$\frac{d^2n}{m_t dm_t dy} = C_1 e^{-(m_t - m)/T} + C_2 e^{-(m_t - m)/T'}. \qquad (1)$$

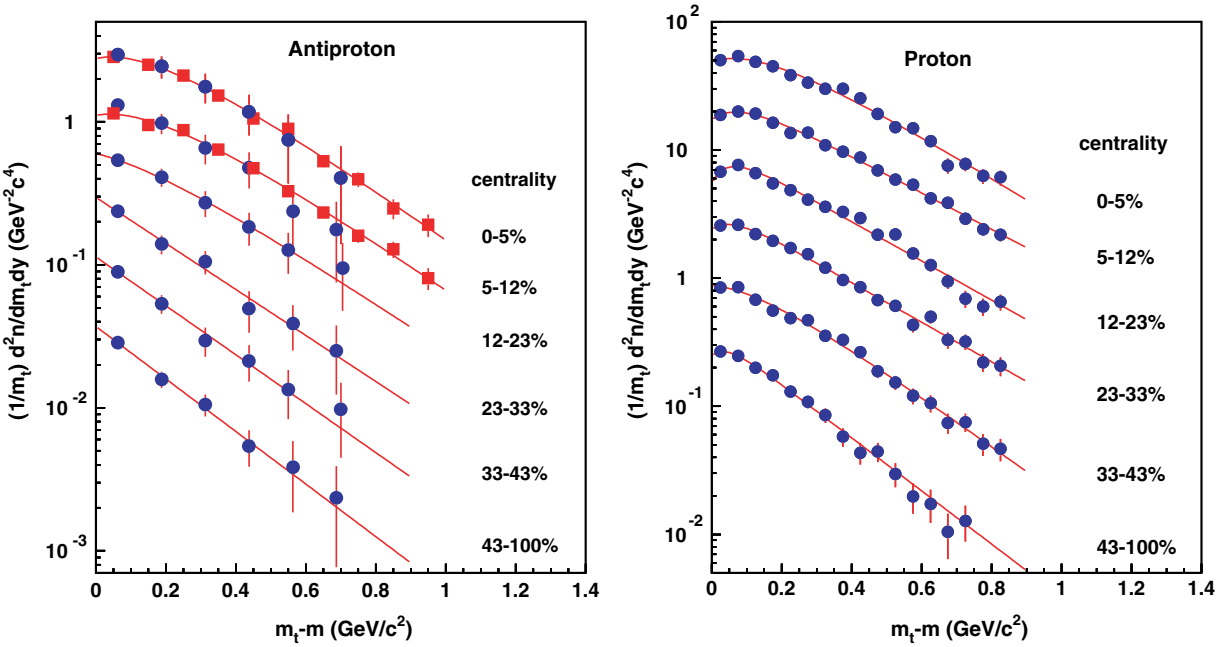

FIG. 2. (Color online) Transverse mass distributions for antiprotons and protons [21] in the rapidity interval $2.4 < y < 2.8$ for the six centrality classes in 158A GeV Pb+Pb collisions. The circle and square points denote the data obtained with the trigger settings selecting minimum bias and central collisions, respectively. Errors are statistical. Curves through the measured points represent the two-exponential fit of Eq. (1) to the data. For clarity, the spectra are scaled down by a factor of 2 successively from the uppermost data.

TABLE II. Particle yield dn/dy, inverse slope T, and mean transverse mass $\langle m_t \rangle - m$ for antiprotons and protons ($2.4 < y < 2.8$) at various centralities in 158A GeV Pb+Pb collisions. Errors are statistical. Proton results are from [21].

	Centrality (% of σ_{inel})	dn/dy	T (MeV)	$\langle m_t \rangle - m$ (MeV/c^2)
$\bar{p}$	0–5	1.66 ± 0.17	291 ± 15	384 ± 19
	5–12	1.27 ± 0.11	299 ± 15	393 ± 16
	12–23	1.05 ± 0.08	274 ± 22	370 ± 45
	23–33	0.76 ± 0.06	269 ± 29	320 ± 35
	33–43	0.55 ± 0.05	255 ± 28	309 ± 32
	43–100	0.33 ± 0.04	236 ± 26	284 ± 28
p	0–5	29.6 ± 0.9	308 ± 9	413 ± 13
	5–12	22.2 ± 0.6	308 ± 9	415 ± 14
	12–23	14.5 ± 0.4	276 ± 9	362 ± 12
	23–33	9.8 ± 0.3	273 ± 10	355 ± 12
	33–43	5.7 ± 0.2	245 ± 10	315 ± 13
	43–100	2.9 ± 0.1	216 ± 10	259 ± 12

A single exponential [first term in Eq. (1)] describes well the data at $m_t - m > 0.2$ GeV/c^2 and determines the inverse slope parameter of the spectra to be discussed further (hereafter denoted by T). The second exponential term with a slope paremeter $T' \approx 100$ MeV accounts for the flattening of the spectra at low m_t. Its contribution to the total yield decreases from nearly 10% in central events to almost zero in the peripheral bins. The double exponential parametrization of Eq. (1) was used for extrapolation to the unmeasured m_t region when calculating the midrapidity yield dn/dy and the mean transverse mass $\langle m_t \rangle - m$. The extrapolation of the antiproton spectra ranges from 8% to 15% for the two most central bins and for the more peripheral bins, respectively. Table II summarizes the results on dn/dy, T, and $\langle m_t \rangle - m$ derived from the $\bar{p}$ and p transverse spectra for each centrality bin of 158A GeV Pb+Pb collisions.

The sources of considered systematic uncertainties include possible errors in the determination of the efficiency corrections, in particular those for selection of single track hits in the TOF pixels as well as the corrections for particle identification and background subtraction. This is only relevant to the antiprotons at higher momenta and high particle multiplicity.

The estimate of the particle yield dn/dy represents an extrapolation into unmeasured regions under the explicit assumption of a certain shape of the m_t distribution. However, the major systematic error arises from uncertainty in the phase space distributions of the parent hyperons decaying into antiprotons. The latter error was derived from the spread of the experimental data on $\bar{\Lambda}$ production used for feeddown corrections including the quoted systematic errors. The overall systematic errors of the antiproton results amount to approximately 10% for the particle yield and 5% for the inverse slope parameter with a weak dependence on centrality of the collision.

Analyses of transverse spectra at the lower SPS energies of 20A, 30A, 40A, and 80A GeV were performed in the same manner as for 158A GeV. Here, the online trigger was set to the 7% most central Pb+Pb collisions which corresponds to the number of wounded nucleons $\langle N_{\text{wound}} \rangle = 345 \pm 28$. The data set comprises about 300 000 events for each energy. Measurements were done near midrapidity and covered the rapidity intervals of $1.5 < y < 2.2$ for 20A GeV ($y_{\text{c.m.}} = 1.88$), $1.6 < y < 2.3$ for 30A GeV ($y_{\text{c.m.}} = 2.08$), $1.9 < y < 2.3$ for 40A GeV ($y_{\text{c.m.}} = 2.22$), and $2.2 < y < 2.6$ for 80A GeV ($y_{\text{c.m.}} = 2.57$).

The geometrical acceptance at lower energies allows us to extend the transverse mass distributions for protons up to $m_t - m = 1.5$ GeV/c^2 ($p_t = 2.25$ GeV/c). Thus, the extrapolation into the unmeasured m_t region is negligibly small. The background contamination due to misidentification of antiprotons at lower energies is less than that at 158A GeV.

Corrections due to the identification cuts applied to dE/dx and m^2 for selection of the $\bar{p}$ samples do not exceed a few percent at the largest values of p and p_t. For the feeddown correction, the NA49 data [22,30] on $\bar{\Lambda}$ and Λ production obtained for the same data samples were used. The $\bar{p}$ feeddown contribution at lower energies became larger as compared to 158A GeV and gradually increased with decreasing beam energy reaching nearly 50% at 20A and 30A GeV. This increases the overall systematic errors toward lower energies, approaching 15% for the antiproton yield at 20A GeV. The feeddown correction for p at low energies amounts to approximately 15%, which is rather close to that for 158A GeV.

Figure 3 depicts the $\bar{p}$ spectra for central Pb+Pb collisions at all five energies together with fits by the double exponential function Eq. (1). A deviation from a single exponential shape is clearly seen. The slope parameter $T' \approx 100$ MeV in the second term of Eq. (1) is almost the same for all five energies. The contribution of this term to the total yield is estimated to be about 10%. The numerical values for dn/dy, T, and $\langle m_t \rangle - m$ are listed in Table III.

IV. DISCUSSION

The midrapidity m_t spectra for 158A GeV Pb+Pb collisions become progressively flatter from peripheral to central

TABLE III. Particle yield dn/dy, inverse slope T, and mean transverse mass $\langle m_t \rangle - m$ for antiprotons and protons in central Pb+Pb collisions at 20A, 30A, 40A, 80A, and 158A GeV beam energies. Errors are statistical.

	E_{beam} (A GeV)	dn/dy	T (MeV)	$\langle m_t \rangle - m$ (MeV/c^2)
$\bar{p}$	158	1.66 ± 0.17	291 ± 15	384 ± 19
	80	0.87 ± 0.07	283 ± 30	385 ± 41
	40	0.32 ± 0.03	246 ± 35	355 ± 51
	30	0.16 ± 0.02	290 ± 45	395 ± 60
	20	0.06 ± 0.01	279 ± 64	394 ± 60
p	158	29.6 ± 0.9	308 ± 9	413 ± 13
	80	30.1 ± 1.0	260 ± 11	364 ± 16
	40	41.3 ± 1.1	257 ± 11	367 ± 16
	30	42.1 ± 2.0	265 ± 10	362 ± 14
	20	46.1 ± 2.1	249 ± 9	352 ± 13

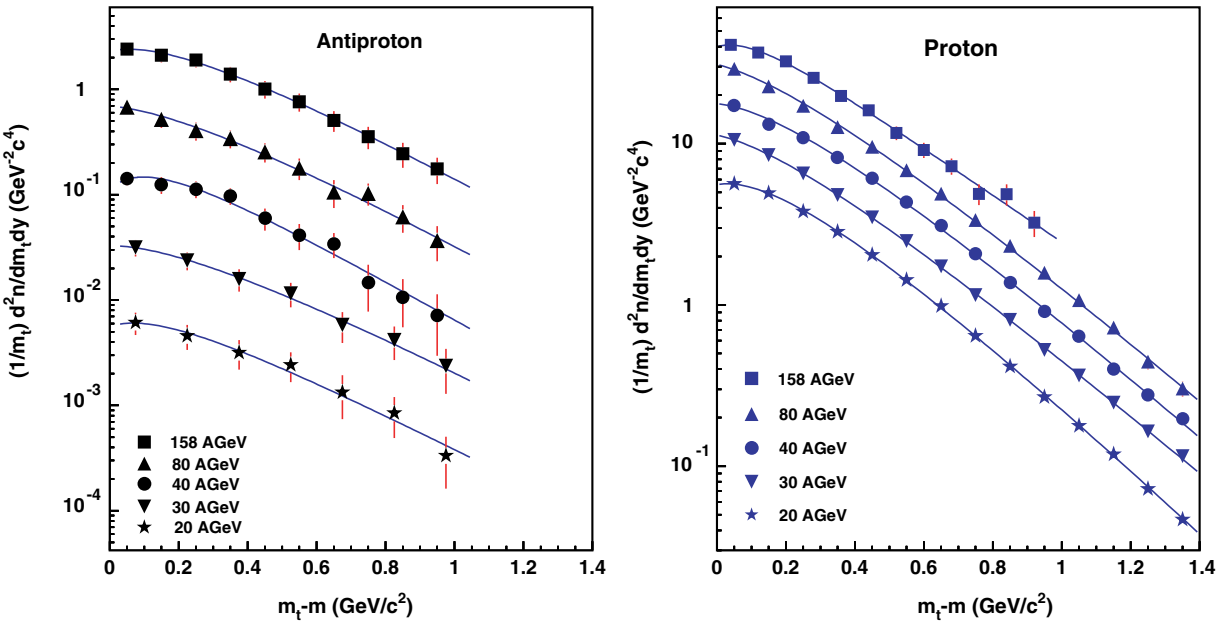

FIG. 3. (Color online) Transverse mass distributions for antiprotons and protons at midrapidity in central Pb+Pb collisions at 20*A*, 30*A*, 40*A*, 80*A*, and 158*A* GeV. Errors are statistical. Solid lines illustrate the two-exponential fit of Eq. (1) to the data. For clarity, the spectra are scaled down by a factor of 2 successively from the uppermost data.

collisions (Fig. 2 and Table II). Both the mean transverse mass $\langle m_t \rangle - m$ and the inverse slope parameter T increase toward central collisions; although this trend is slightly different for $\bar{p}$ and p, namely, the proton inverse slope increases somewhat faster, as clearly seen in Fig. 4.

A deviation from a single exponential at low m_t values, the so-called shoulder-arm shape, is most pronounced in central

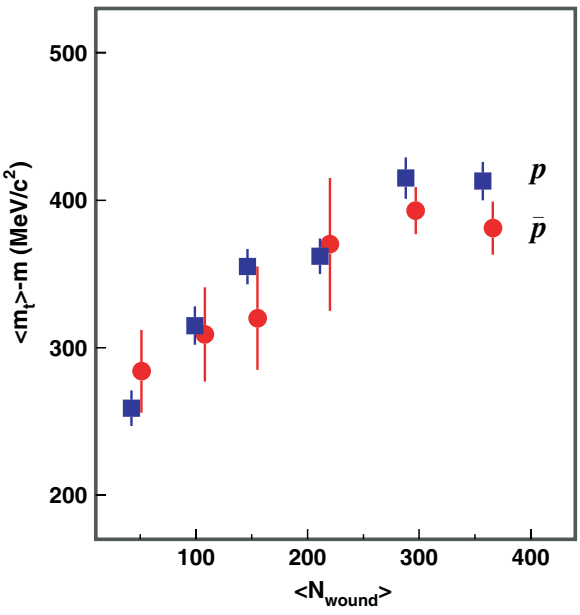

FIG. 4. (Color online) Mean transverse mass $\langle m_t \rangle - m$ for $\bar{p}$ and p as a function of N_{wound} at midrapidity in 158*A* GeV Pb+Pb collisions. Errors are statistical.

Pb+Pb collisions (Fig. 2) and observed at all five energies (Fig. 3). These features are generally explained by a strong collective expansion (radial flow) in hydrodynamic models [31–33]. A blast wave parametrization based on these models provides in fact as good a description of the m_t spectra [34] as the double exponential function. Fitted parameters yield an average radial flow velocity of about $0.5c$ and a temperature of 120–140 MeV in the expanding fireball at its disintegration stage.

Interestingly, the $\bar{p}$ and p transverse mass spectra reveal within errors quite similar shapes, even though at these energies a significant fraction of protons carry the baryon number from the incoming nuclei, while antiprotons are predominantly pair produced. This observation may indicate similar expansion dynamics comprised of both thermal motion and collective radial flow, which determine the transverse spectra of particles at the late stage of the expansion. As discussed in the Introduction, substantial annihilation of primordially produced $\bar{p}$ might occur in the baryon rich fireball. This effect is expected to lead to a decrease of the $\bar{p}/p$ ratio at $m_t - m$ below about 0.4 GeV/c^2 [15,17]. In particular, at 158*A* GeV the close similarity of the shapes of the measured $\bar{p}$ and p spectra does not support such a prediction. At lower energies, a decrease of the order of 30% cannot be ruled out because of the larger uncertainties of the measurements.

In contrast to the strong centrality dependence, the shape of the measured transverse mass spectra does not change noticeably with beam energy at SPS energies. This is illustrated in Fig. 5, where the $\langle m_t \rangle - m$ values for p and $\bar{p}$ in central Pb+Pb collisions at the five SPS energies are plotted vs the nucleon-nucleon center-of-mass energy. Also shown are measurements at lower and higher energies from the AGS

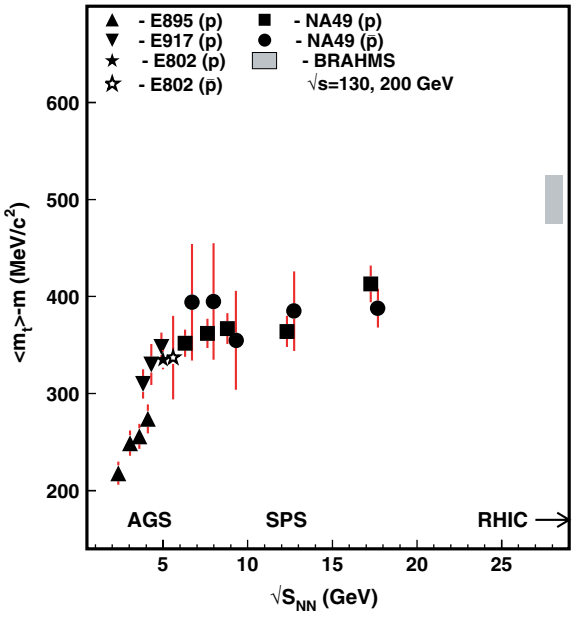

FIG. 5. (Color online) Mean transverse mass $\langle m_t \rangle - m$ for $\bar{p}$ and p at midrapidity as a function of the c.m. energy per nucleon pair $\sqrt{s_{NN}}$ in central Pb+Pb collisions at SPS energies (NA49) together with data for central Au+Au collisions from the AGS [35–37] and RHIC [38]. Errors are statistical.

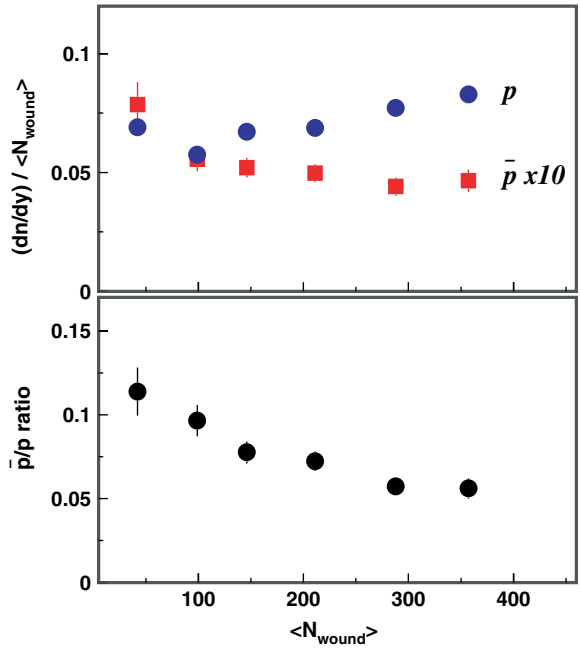

FIG. 6. (Color online) Yield dn/dy of $\bar{p}$ and p per N_{wound} and the $\bar{p}/p$ ratio plotted as a function of N_{wound} at midrapidity in 158A GeV Pb+Pb collisions. Errors are statistical.

[35–37] and RHIC [38], respectively. It is seen that the mean transverse mass for both $\bar{p}$ and p steeply rises with energy at the AGS, remains approximately constant at the SPS, and resumes a slow rise toward RHIC energies. A similar nontrivial energy dependence was also observed by NA49 for kaon and pion production [30], which was considered a possible manifestation of the coexistence of partonic and hadronic phases or more generally a very soft equation of state in the SPS energy regime [39–41]. The behavior of the m_t spectra may thus be taken to support the indication of an onset of deconfinement in the early stage of the collisions at low SPS energies as obtained from the energy dependence of pion and kaon yields [19].

The measured particle yields dn/dy differ significantly between p and $\bar{p}$. Both increase with increasing centrality, but the proton yield rises about two times faster. The yields of p and $\bar{p}$ per wounded nucleon $(dn/dy)/\langle N_{\text{wound}} \rangle$ as a function of N_{wound} for the six centrality samples are depicted in Fig. 6. An increase of this ratio with centrality for protons is seen, which can be understood as a consequence of the increased baryon stopping in central Pb+Pb collisions [26–28]. On the other hand, the $\bar{p}$ yield per wounded nucleon shows a decrease with increasing centrality. This could be a sign of increasing antiproton absorption in central collisions. This effect was studied with the microscopic models UrQMD [17] and HSD [5] which comprise string excitation, hadronization, and rescattering (transport) stages. The UrQMD results [17] suggest a concurrence of the $\bar{p}$ enhancement in Pb+Pb collisions with respect to p+p reactions and an increasing antibaryon absorption with centrality due to the growth of the net baryon density at midrapidity. However, the observation of nearly identical spectra for p and $\bar{p}$ does not support the UrQMD model calculation. The HSD model explains the weak centrality dependence of the $\bar{p}$ yield per wounded nucleon by the contribution of multimeson reactions in the transport phase [5]. These regenerate $\bar{p}$, and thus counteract the loss by absorption.

The different dependence of $\bar{p}$ and p yields on N_{wound} results in significant centrality dependence of the $\bar{p}/p$ ratio as shown in the bottom panel of Fig. 6. This ratio steadily decreases with centrality by a factor of about 2 within the considered centrality range. A similar result was obtained in Au+Au collisions at 11.7A GeV [37]. The latter reaction is on the lead, so it has to be an even larger $\bar{p}/p$ ratio than observed in peripheral Pb+Pb reactions reaching values of nearly 0.3 for p+p [42] and p+Pb [43] interactions. In contrast, the $\bar{p}/p$ ratio measured at RHIC shows very weak variation with centrality at the collision energy $\sqrt{s_{NN}} = 130$ GeV [44,45] and almost no dependence on centrality at $\sqrt{s_{NN}} = 200$ GeV [46,47]. Thus, the net baryon density, which is significant at lower energies, strongly affects the midrapidity p and $\bar{p}$ abundances through baryon stopping and baryon-antibaryon annihilation in central collisions at the AGS and SPS, but not at RHIC energies.

Figure 7 displays the midrapidity $\bar{p}/p$ ratio for central collisions as a function of energy at AGS, SPS, and RHIC. The numerical values are listed in Table IV. The $\bar{p}/p$ ratio rises steeply within the SPS energy range by nearly two orders of magnitude. The figure illustrates how the collisions evolve from producing a net baryon-rich system at the AGS through the SPS energy range to an almost net baryon-free midrapidity region at the RHIC.

Measurements of $\bar{\Lambda}$ production in central Pb+Pb collisions [22,30] make it possible to analyze strange and nonstrange antibaryon production for all five beam energies. Of particular

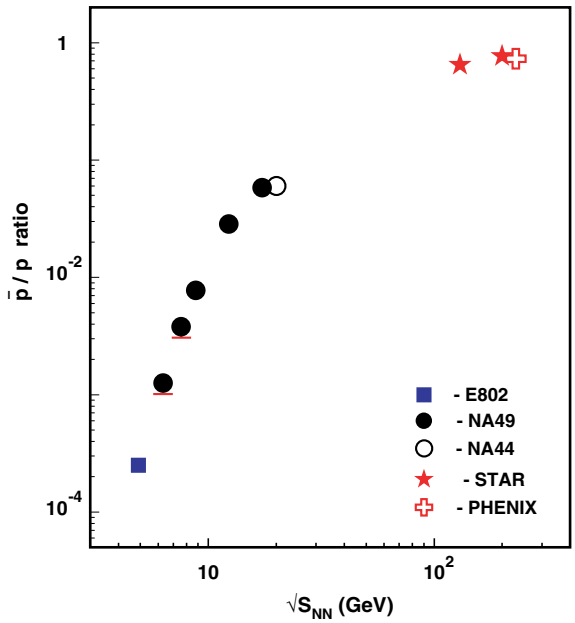

FIG. 7. (Color online) The $\bar{p}/p$ ratio at midrapidity as a function of the c.m. energy per nucleon pair $\sqrt{s_{NN}}$ in central Pb+Pb collisions at SPS energies (NA49) together with the data for lower energies at the AGS [37] and higher energies at the RHIC [44,45,47], respectively. The data [48] at top SPS energy are also shown.

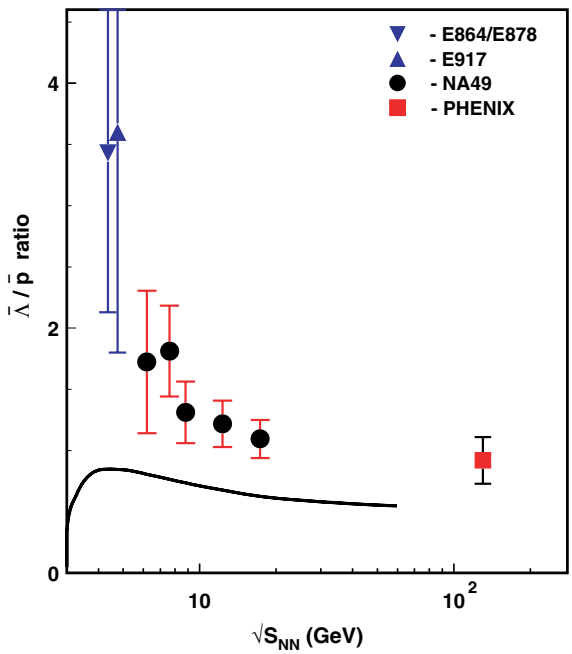

FIG. 8. (Color online) $\bar{\Lambda}/\bar{p}$ ratio at midrapidity as a function of the c.m. energy per nucleon pair $\sqrt{s_{NN}}$ in central Pb+Pb collisions at SPS energies (NA49) together with data from AGS [7,8] and RHIC [11]. Total error bars are drawn. Curve shows the prediction of the statistical hadron gas model [49].

interest is the $\bar{\Lambda}/\bar{p}$ ratio which was briefly discussed in the Introduction. Note that the $\bar{\Lambda}$ yields used for calculations contain the contribution from electromagnetic decays of $\bar{\Sigma}^0$ hyperons, which are experimentally indistinguishable from those created in primary interactions.

The measured values of the $\bar{\Lambda}/\bar{p}$ ratio for central Pb+Pb collisions at 20*A*, 30*A*, 40*A*, 80*A*, and 158*A* GeV are listed in Table IV and plotted in Fig. 8, together with those from AGS and RHIC. The AGS experiments reported a $\bar{\Lambda}/\bar{p}$ ratio of about 3–3.5 for central Au+Au [7,8] and Si+Au [9] collisions at beam momenta of 11.7*A* and 14.6*A* GeV/*c*, respectively. As illustrated in Fig. 8, the measurements at the SPS indicate a gradual increase of the $\bar{\Lambda}/\bar{p}$ ratio from 158*A* GeV to 30*A* and 20*A* GeV, and tend to corroborate the large values for this ratio found at AGS energies. At 158*A* GeV, the published prediction [18] for the midrapidity $\bar{\Lambda}/\bar{p}$ ratio from the UrQMD model, which takes into account antibaryon absorption, agrees well with the measured value. Predictions for the full energy range are not yet available in the literature. Since both $\bar{\Lambda}$ and $\bar{p}$ are newly produced baryons having no valence quarks in common with the projectile nucleons, we may compare the midrapidity ratio with the full phase space multiplicity ratio predicted by the statistical hadron gas model [49] which uses a smooth parametrization of the energy dependence of the baryochemical potential. As demonstrated by the curve in Fig. 8, the hadron gas model underpredicts the ratio but shows a rise toward lower energies similar to the measurements. Similar predictions were obtained within nonequilibrium versions of the hadron gas model [50,51].

TABLE IV. The $\bar{p}/p$ and $\bar{\Lambda}/\bar{p}$ ratios at midrapidity in central Pb+Pb collisions at SPS energies. Errors are statistical. Preliminary results for $\bar{\Lambda}$ yields at 20*A* and 30*A* GeV [30] are used.

E_{beam} (*A* GeV)	$\bar{p}/p$	$\bar{\Lambda}/\bar{p}$
158	0.058 ± 0.005	1.09 ± 0.15
80	0.028 ± 0.003	1.22 ± 0.14
40	0.0078 ± 0.0010	1.31 ± 0.19
30	0.0038 ± 0.0008	1.81 ± 0.37
20	0.0013 ± 0.0002	1.72 ± 0.58

The increase of the $\bar{\Lambda}/\bar{p}$ ratio toward top AGS energies may also find an explanation in a quark coalescence model scenario. Note first of all that we deal here with an antihyperon to antiproton maximum because this ratio has to fall down again at yet lower energies (where no data exist due to insufficient statistics) owing to the higher $\bar{\Lambda}$ production threshold. Such an antihyperon maximum is reminiscent of the maximum in the same energy range that was reported recently for the K^+/π^+ production ratio [19,20]. The steep maximum in the relative strangeness production was predicted as a signal of the onset of deconfinement [52]. In fact, if hadronization occurs by quark coalescence at the QGP phase boundary, the $\bar{\Lambda}/\bar{p}$ ratio essentially reflects the ratio of $\bar{s}$ to $\bar{u}$ quark densities, while the K^+/π^+ ratio follows from the $\bar{s}$ to $\bar{d}$ ratio. The $\bar{d}$ quark density is expected to be proportional, in turn, to the $\bar{u}$ quark density. These considerations thus provide a possible explanation of the similar rise in the $\bar{\Lambda}/\bar{p}$ and K^+/π^+ ratios with decreasing collision energy.

For 158*A* GeV, Pb+Pb collisions, the data allow a study of the centrality dependence of the midrapidity $\bar{\Lambda}/\bar{p}$ ratio which

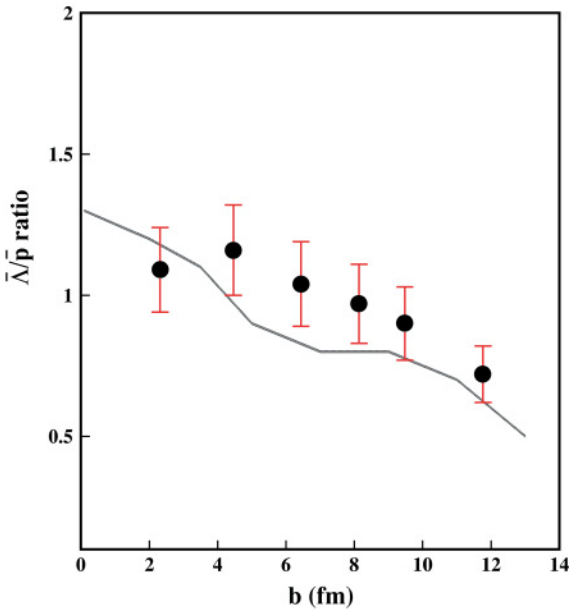

FIG. 9. (Color online) Impact parameter dependence of the $\bar{\Lambda}/\bar{p}$ ratio at midrapidity in central Pb+Pb collisions at 158*A* GeV. Errors are statistical. Curve presents the result of hadronic cascade (UrQMD) calculation [18].

has been suggested to be particularly sensitive to the interplay between production and subsequent absorption. As data on the centrality dependence of $\bar{\Lambda}$ production are not yet available from NA49, numerical values for the ratio were derived from the yield of $\bar{\Lambda}$ in the most central bin 1 measured by NA49 [22] and the calculated yields for centrality bins 2–6 using the NA57 result [23] that the $\bar{\Lambda}$ yield within the errors is proportional to the number of wounded nucleons N_{wound}. As shown in Fig. 9, the $\bar{\Lambda}/\bar{p}$ ratio increases from peripheral to central collisions by about a factor of 2. A much stronger increase with centrality has been observed at the AGS [7,8]. Interestingly, the results at 158*A* GeV are in agreement with a UrQMD model calculation [18] which incorporates antibaryon absorption.

V. SUMMARY

The midrapidity transverse mass distributions for antiprotons were measured in Pb+Pb collisions at 20*A*, 30*A*, 40*A*, 80*A*, and 158*A* GeV filling the gap in the data between the AGS and top SPS energies. They are compared to the relevant data for proton and antilambda production.

The shapes of m_t spectra show a strong dependence on collision centrality. In central collisions and at small m_t, the spectra exhibit a pronounced deviation from the exponential Boltzmann shape. The data reveal the shoulder-arm structure characteristic of prominent radial collective expansion flow. The observation of a nearly identical spectral shape for antiprotons and protons indicates a similar expansion history for both particle species.

No visible change in the mean transverse mass for $\bar{p}$ and p was found in central Pb+Pb collisions within the measured SPS energy range. This is similar to what has been observed in kaon and pion production and could be attributed to the possible formation of a deconfined phase in the early stage of the collision.

The yield of p normalized to the number of wounded nucleons increases with centrality, while this quantity for $\bar{p}$ exhibits a decrease. The former effect can be understood as the result of an increase of baryon stopping with collision centrality which leads to contraction of the proton rapidity distribution around midrapidity. The decrease of the yield of $\bar{p}$ per wounded nucleon may point to some contribution from annihilation.

The $\bar{p}/p$ ratio is found to increase by almost two orders of magnitude in central Pb+Pb collisions at 158*A* GeV as compared to 20*A* GeV beam energy, reflecting the rapid decrease of the net baryon density at midrapidity with collision energy.

In central Pb+Pb collisions, the $\bar{\Lambda}/\bar{p}$ ratio shows a steady increase with decreasing beam energy approaching a value of almost 2 at the energies of 20*A* and 30*A* GeV. This confirms earlier evidence for this ratio to significantly exceed unity at AGS energies. There may be an analogy to the K^+/π^+ maximum also observed in the domain of top AGS to lowest SPS energies.

No fully satisfactory theoretical description of antibaryon production is available in the literature. The new experimental results on $\bar{p}$ production should help elucidate the possible role of annihilation processes in antihyperon production in collisions of heavy nuclei.

ACKNOWLEDGMENTS

This work was supported by the U.S. Department of Energy Grant DE-FG03-97ER41020/A000, the Bundesministerium fur Bildung und Forschung, Germany, the Virtual Institute VI-146 of Helmholtz Gemeinschaft, Germany, the Polish State Committee for Scientific Research (1 P03B 097 29, 1 P03B 121 29, 2 P03B 04123), the Hungarian Scientific Research Foundation (T032648, T032293, T043514), the Hungarian National Science Foundation, OTKA (F034707), the Polish-German Foundation, the Korea Research Foundation Grant (KRF-2003-070-C00015), and the Bulgarian National Science Fund (Ph-09/05).

[1] P. Koch, B. Müller, H. Stöcker, and W. Greiner, Mod. Phys. Lett. **A8**, 737 (1988); J. Ellis, U. Heinz, and H. Kowalski, Phys. Lett. **B233**, 223 (1989); U. Heinz, P. R. Subramanian, H. Stöcker, and W. Greiner, J. Phys. G: Nucl. Part. Phys. **12**, 1237 (1986).

[2] J. Rafelski and B. Müller, Phys. Rev. Lett. **48**, 1066 (1982); J. Rafelski, Phys. Rep. **88**, 331 (1982); P. Koch, B. Müeller, and J. Rafelski, *ibid.* **142**, 167 (1986).

[3] P. Koch and C. B. Dover, Phys. Rev. C **40**, 145 (1989); S. Gavin, M. Gyulassy, M. Plümer, and R. Venugopalan, Phys. Lett. **B234**, 175 (1982).

[4] R. Rapp and E. V. Shuryak, Phys. Rev. Lett. **86**, 2980 (2001).
[5] W. Cassing, Nucl. Phys. **A700**, 618 (2002).
[6] T. Alber *et al.* (NA35 Collaboration), Phys. Lett. **B366**, 56 (1996).
[7] B. B. Back *et al.* (E917 Collaboration), Phys. Rev. Lett. **87**, 242301 (2001).
[8] T. A. Armstrong *et al.* (E864 Collaboration), Phys. Rev. C **59**, 2699 (1999); T. A. Armstrong *et al.* (E864 Collaboration), Phys. Rev. Lett. **79**, 3351 (1997); D. Beavis *et al.* (E878 Collaboration), *ibid.* **75**, 3633 (1995).
[9] G. S. F. Stephans *et al.* (E859 Collaboration), J. Phys. G: Nucl. Part. Phys. **23**, 1895 (1997).
[10] A. Mischke (NA49 Collaboration), Nucl. Phys. **A715**, 453c (2003).
[11] K. Adcox *et al.* (PHENIX Collaboration), Phys. Rev. Lett. **89**, 092302 (2002).
[12] J. Rafelski and M. Danos, Phys. Rev. C **50**, 1684 (1994).
[13] F. Becattini, J. Cleymans, A. Keranen, E. Suhonen, and K. Redlich, Phys. Rev. C **64**, 024901 (2001).
[14] G. J. Wang, G. Welke, R. Bellwied, and C. Pruneau, arXiv:nucl-th/9807036.
[15] F. Wang, J. Phys. G: Nucl. Part. Phys. **27**, 283 (2001).
[16] F. Wang, arXiv:nucl-ex/9905005 (1999).
[17] M. Bleicher *et al.*, Phys. Lett. **B485**, 133 (2000); X. Zhu, UrQMD group, private communication.
[18] M. Bleicher, M. Reiter, A. Dumitru, J. Brachmann, C. Spieles, S. A. Bass, H. Stocker, and W. Greiner, Phys. Rev. C **59**, R1844 (1999); S. A. Bass *et al.*, Prog. Part. Nucl. Phys. **41**, 225 (1998); X. Zhu, UrQMD group, private communication: The results from later versions of UrQMD show the same trend, but lower values of the $\bar{\Lambda}/\bar{p}$ ratio.
[19] S. V. Afanasiev *et al.* (NA49 Collaboration), Phys. Rev. C **66**, 054902 (2002).
[20] M. Gaździcki (NA49 Collaboration), J. Phys. G: Nucl. Part. Phys. **30**, 701 (2004).
[21] T. Anticic *et al.* (NA49 Collaboration), Phys. Rev. C **69**, 024902 (2004).
[22] T. Anticic *et al.* (NA49 Collaboration), Phys. Rev. Lett. **93**, 022302 (2004).
[23] F. Antinori *et al.* (NA57 Collaboration), Nucl. Phys. **A715**, 140c (2003).
[24] S. V. Afanasiev *et al.* (NA49 Collaboration), Nucl. Instrum. Methods Phys. Res. A **430**, 210 (1999).
[25] R. J. Glauber and G. Matthiae, Nucl. Phys. **B21**, 135 (1970).
[26] G. E. Cooper (NA49 Collaboration), Nucl. Phys. **A661**, 362c (1999).
[27] F. Siklér *et al.* (NA49 Collaboration), Nucl. Phys. **A661**, 45c (1999).
[28] H. Appelshäuser *et al.* (NA49 Collaboration), Phys. Rev. Lett. **82**, 2471 (1999).
[29] H. Sorge, Phys. Rev. C **52**, 3291 (1995).
[30] Ch. Blume *et al.* (NA49 Collaboration), J. Phys. G: Nucl. Part. Phys. **31**, 685 (2005); Ch. Meurer (NA49 Collaboration), *ibid.* **30**, 1325 (2004).
[31] H. Sorge, J. L. Nagle, and B. S. Kumar, Phys. Lett. **B355**, 27 (1995); J. Sollfrank *et al.*, Z. Phys. C **52**, 593 (1991); U. Heinz, Nucl. Phys. **A610**, 264c (1996).
[32] U. Heinz *et al.*, Phys. Lett. **B382**, 181 (1996); S. Chapman, J. R. Nix, and U. Heinz, Phys. Rev. C **52**, 2694 (1995).
[33] P. Braun-Munzinger, J. Stachel, J. P. Wessels, and N. Xu, Phys. Lett. **B344**, 43 (1995); E. Schnedermann, J. Sollfrank, and U. Heinz, Phys. Rev. C **48**, 2462 (1993); H. Appelshäuser *et al.* (NA49 Collaboration), Eur. Phys. J. C **2**, 661 (1998).
[34] M. van Leeuwen *et al.* (NA49 Collaboration), Nucl. Phys. **A715**, 161c (2003); C. Alt *et al.* (NA49 Collaboration), Phys. Rev. Lett. **94**, 192301 (2005).
[35] J. L. Klay *et al.* (E895 Collaboration), Phys. Rev. Lett. **88**, 102301 (2002).
[36] B. B. Back *et al.* (E917 Collaboration), Phys. Rev. C **66**, 054901 (2002).
[37] I. Ahle *et al.* (E802 Collaboration), Phys. Rev. Lett. **81**, 2650 (1998).
[38] I. Arsene *et al.* (BRAHMS Collaboration), Nucl. Phys. **A757**, 1 (2005).
[39] L. van Hove *et al.*, Phys. Lett. **B118**, 138 (1982).
[40] M. Gorenstein *et al.*, Phys. Lett. **B567**, 175 (2003).
[41] B. Mohanty, Jan-e Alam, S. Sarkar, T. K. Nayak, and B. K. Nandi, Phys. Rev. C **68**, 021901(R) (2003).
[42] K. Guettler *et al.*, Phys. Lett. **64B**, 111 (1976).
[43] I. G. Bearden *et al.* (NA44 Collaboration), Phys. Rev. C **57**, 837 (1998).
[44] C. Adler *et al.* (STAR Collaboration), Phys. Rev. Lett. **86**, 4778 (2001).
[45] K. Adcox *et al.* (PHENIX Collaboration), Phys. Rev. C **69**, 024904 (2004).
[46] J. Adams *et al.* (STAR Collaboration), Phys. Rev. Lett. **92**, 112301 (2004).
[47] S. S. Adler *et al.* (PHENIX Collaboration), Phys. Rev. C **69**, 034909 (2004).
[48] M. Kaneta *et al.* (NA44 Collaboration), J. Phys. G: Nucl. Part. Phys. **23**, 1865 (1997).
[49] J. Cleymans and K. Redlich, Phys. Rev. Lett. **81**, 5284 (1998).
[50] F. Becattini, J. Manninen, and M. Gaździcki, arXiv:hep-ph/0511092.
[51] J. Letessier and J. Rafelski, arXiv:nucl-th/0504028, Phys. Rev. C (to be published).
[52] M. Gaździcki and M. Gorenstein, Acta Phys. Pol. B **30**, 2705 (1999) [arXiv:hep-ph/9803462].